1 **Title: Environmental sensing in dynamic quorum responses**

2

3 **Authors:** Eric K. Chu[1,2,3], Alex Groisman[4] and Andre Levchenko[1,2,3,*]

4 **Affiliations (at the time the work was performed):**

5   1. Department of Biomedical Engineering, Yale University, New Haven, Connecticut 06520,

6   USA

7   2. Yale Systems Biology Institute, Yale University, West Haven, Connecticut 06516, USA

8   3. Department of Biomedical Engineering, The Johns Hopkins University School of

9   Medicine, Baltimore, Maryland 21205, USA

10   4. Department of Physics, University of California, San Diego, La Jolla, California 92093,

11   USA

12   * Please address the correspondence to andre.levchenko@yale.edu

13

14 **Abstract**

15 Cell communication and coordinated cell behavior are hallmarks of multicellular behavior of

16 living systems. However, in many cases, including the ancient and archetypal example of

17 bacterial quorum sensing, the meaning of the communicated information remains a subject of

18 debate. It is commonly assumed that quorum sensing encodes the information on the current

19 state of the colony, including cell density and physical colony confinement. Here, we show that

20 quorum sensing can also be exquisitely sensitive to dynamic changes in the environment,

21 including fluctuations of the prevailing nutrient source. We propose a new signaling mechanism

22 accounting for this sensory capability. This mechanism combines regulation by the commonly

23 studied *lux* operon-encoded network with the environmentally determined balance of protein

24 synthesis and dilution rates, dependent on the rate of cell proliferation. This regulatory

25 mechanism accounts for observed complex spatial distribution of quorum responses, and

26 emergence of sophisticated processing of dynamic inputs, including temporal thresholds and

27 persistent partial induction following a transient change in the environmental conditions. We

28 further show that, in this context, cell communication in quorum sensing acquires a new

29 meaning: education of cells within a population about the past history of transient exposure to

30 adverse conditions by a subset of induced cells. In combination, these signaling and

31 communication features may endow a cell population with increased fitness in diverse

32 fluctuating environments.

33

34   **Introduction**

35   Collective cell behaviors coordinated by inter-cellular communication are ubiquitous across all

36   domains of life[1-5], supporting evolutionary advantages of multicellular vs. cell-autonomous

37   signal detection and responses. However, the information conveyed in cell-cell communication

38   and its consequences for the population fitness in dynamically changing environments are

39   frequently not known. Quorum sensing (QS) is an ancient archetypal cell-cell communication

40   mechanism found in many prokaryotes[6]. It is used to coordinate collective cell responses,

41   through endogenously-produced diffusible molecules called autoinducers (AI)[7,8]. What exactly is

42   sensed in the process of QS, however, is a matter of debate. Classically, QS has been defined as a

43   means to condition adaptive responses on achieving sufficient cell density (CD), which is gauged

44   by the accumulation of AI with increasing cell number[9,10]. However, AI can also accumulate to

45   high levels due to poor diffusive characteristics of the local environment, even if the cell density

46   is relatively low[11,12]. This observation led to an alternative interpretation of AI-mediated QS

47   signaling as an active method of surveying the diffusive (DF) transport characteristics of the

48   extracellular milieu[13]. Importantly, QS is frequently coupled to stress-response phenotypes such

49   as sporulation[14,15], virulence[16-18], and biofilm formation[19-21], indicating that at least some aspects

50   of QS can report on adverse environmental conditions. Indeed, poor local diffusive properties or

51   high cell density might also hamper nutrient availability[22]; however, neither CD nor DF sensing

52   interpretations directly relate to the detection of changes in the environmental conditions,

53   particularly of subtle fluctuations in nutrient content. It is not clear, therefore, whether QS might

54   in fact be a mechanism to sense dynamic changes in the potentially stressful, dynamic cell

55   microenvironment[23], or it just enables this sensing (e.g., in a cell density-dependent fashion)

56   through alternative sensory mechanisms[24].

57

58   To explore the function of QS, it is important to investigate the dynamic features of QS

59   responses. However, the emphasis has traditionally been placed on the categorical on or off

60   description, stemming from the common feature of the molecular circuits underlying QS – the

61   positive feedback. Positive autoregulation is observed, for example, in a frequently studied QS

62   circuit of the marine bacterium *V. fischeri*, whose response is controlled by the *lux* operon[25]. It

63   involves AI, produced by the AI synthase LuxI, binding to its cognate cytoplasmic AI receptor

64   LuxR, and positively auto-regulating the *LuxI* and *LuxR* in addition to driving bioluminescence

65   gene transcription[26-28]. This simple feedback regulatory circuit enables a switch-like increase in

66   the QS response after the threshold concentration of AI is exceeded[29]. However, the time scale of

67   this response and its single-cell properties remain poorly understood. It is therefore not clear how

68   the dynamics of QS may compare to other key time scales, including the duration of cell cycle,

69   environmental fluctuations or, for example, in the case of *V. fischeri*, the day-night life cycle of

70   the host (i.e., the Hawaiian Bobtail Squid, *Euprymna scolopes*).

71

72   Here, using a highly integrated combination of experimental and computational approaches,

73   relying in particular on a new method to tightly control the coupling between bacterial

74   populations and variable environmental conditions, we found several unexpected properties of

75   QS. In particular, we found that QS cannot be fully accounted for by the current CD and DF

76   sensing theories, thus requiring a new framework for its interpretation. We propose such a

77   framework and provide extensive quantitative evidence for its validity. Furthermore, we find that

78   dynamic, rather than static, QS response can be a critical determinant of the corresponding

79   phenotypic outcomes. In addition, our results suggest that QS can display complex patterns of

4

80   spatial distribution and variability, allowing for an increased fitness in the uncertain

81   environments, through a communication-driven cell 'education' mechanism. These findings can

82   have important consequences for our understanding of QS and the related phenotypic outcomes,

83   and can have implications for other QS-like phenomena, including eukaryotic community effects

84   and other cell communication-related behaviors.

85

86   **Results**

87   **QS is defined by a balance between nutrient-defined protein synthesis and dilution due to**

88   **cell proliferation**

89   To explore whether QS is consistent with either the CD or DF interpretation **(Fig. 1a)**, we

90   studied the QS responses of densely packed colonies of *E. coli* lab strain MG02S [30] exposed to

91   various tightly-controlled environments within a microfluidic device. MG02S carries a single,

92   genomically integrated copy of *V. fisheri* LuxIR QS circuit regulating GFP expression in lieu of

93   bioluminescence genes **(Fig. 1b)**. The cells were grown to a completely dense monolayer state

94   within 720 microchambers of identical dimensions, but with variable numbers and sizes of

95   connective channels which modulate the diffusive coupling between the microchambers and the

96   medium-supplying flow-through channels **(Fig. 1c, e, Fig. S1a, b)**. We found that, despite

97   achieving dense colonies of ~4000 cells each that were grown chemostatically for 24 hours, cells

98   exhibited no detectable QS in the presence of glucose-rich (20 mM) tryptone-complemented

99   medium (TCM) at 25°C **(Fig. S2a, Movie 1)**. However, switching to glucose-deficient TCM

100   elicited a strong auto-induced QS response, consistent with previous reports of glucose-mediated

101   repression of the *lux* operon[31,32]. Furthermore, despite the same cell density and number within

102   each chamber, the magnitude of QS responses across chambers varied for different coupling

5

103   configurations **(Fig. 1d, S3)**. Thus, the QS responses was not fully consistent with the CD

104   interpretation, but might instead have reflected DF sensing, in which QS response is defined by

105   the diffusion-limited local accumulation of AI. We indeed confirmed that different

106   environmental coupling of individual chambers resulted in variable transport **(Fig. S1c, d, Movie**

107   **2, 3)** and cell growth rates **(Fig. 1e, Fig. S1e-g, Movie 4)**. The transport and cell growth were

108   closely related to each other **(Fig. S1h)**, suggesting that diffusive coupling controlled both AI

109   accumulation and cell proliferation via nutrient access. However, contrary to what was expected

110   from the DF sensing interpretation, the magnitude of QS induction (at 24 hours following the

111   medium switch) was not a monotonic decreasing function, but rather exhibited a biphasic

112   dependence on cell growth rate (and diffusive coupling), **(Fig. 1f, i, Movie 5)**, with the response

113   maximized at intermediate growth rates.

114

115   Further, to directly test whether differential AI accumulation between chambers was responsible

116   for the different QS responses, as would be predicted by the DF sensing hypothesis, we repeated

117   the experiment in the presence of 1 μM of exogenous AI, which is expected to saturate the

118   circuit and thus result in uniform QS induction across different chambers. Unexpectedly,

119   induction with exogenous AI again resulted in a biphasic QS induction pattern, essentially

120   identical to that resulting from auto-induction, albeit with different kinetics **(Fig. 1i, Fig. S2b,**

121   **Movie 6)**, suggesting that neither CD nor DF sensing hypothesis was sufficient to explain the

122   observed responses.

123

124   Since QS response varied with cell growth rate, we tested whether it would change with another

125   source of nutrients. Strikingly, replacing tryptone with a very similar nutrient source, casamino

6

126   acids (tryptone results from partial and casamino acids from complete digestions of casein,

127   respectively), resulted in a very distinct, more homogeneous response distribution, albeit still

128   biphasic in shape, for both auto- and exogenous AI induction conditions **(Fig. 1i)**. Even more

129   surprising, given the similarity of the nutrients, was the dramatically different dynamics of the

130   QS response in the presence of TCM vs. casamino acid complemented medium (CACM) **(Fig.**

131   **1g, Fig. S2c, S4a, b, Movie 7-9)**.

132

133   Our results suggest that neither CD nor DF interpretation is completely adequate to account for

134   the observed QS responses, with the growth rate being a more predictive determinant of the

135   response than either cell density or local accumulation of AI. An explanation of this growth

136   dependency might be provided by the dynamics of QS response, and in particular, the

137   observation that the time scales of QS are comparable to and can exceed the duration of the cell

138   cycle. Therefore, the dynamics and amplitude of the response can be strongly influenced not only

139   by the biochemical interactions within the molecular QS circuit, as is commonly assumed, but

140   also by the dynamic balance between protein synthesis and growth-mediated protein dilution

141   **(Fig. 1h)**. We indeed found that the synthesis and dilution (which can also be converted to

142   protein retention, as shown here) of QS-regulated protein (GFP) were monotonically increasing

143   functions of the cell growth rate **(Fig. 1j)** for both tryptone and casamino acids as nutrient

144   sources. However, the average growth rate was higher and synthesis rate was lower for the

145   tryptone vs. casamino acids complemented media. To test whether the balance of QS protein

146   synthesis and dilution would be able to account for various experimentally observed response

147   dynamics, we modified previously published mathematical models of QS response[33,34] to

148   incorporate the measured synthesis and dilution parameters from the different conditions **(Fig.**

7

149 **S5)**. By matching the synthesis and dilution rate constants to the experimentally estimated

150 values, we obtained the predicted QS dynamics that was consistent with the experimental

151 observations for both nutrient sources **(Fig. 1f, g, Fig. S6)**. This result provided first evidence for

152 the key influence of the balance between protein synthesis and dilution as a regulatory

153 mechanism of the environmental sensitivity of the QS response.

154

155 **Information about distinct environmental conditions is reflected in QS response dynamics**

156 To further support the protein synthesis/dilution balance (PSD) mechanism, we explored QS

157 under additional environmental perturbations. In particular, we reasoned that increasing the

158 temperature would accelerate cell growth and thus increase protein dilution, leading to an

159 attenuated QS response. Indeed, increasing the temperature from 25°C to 30°C elevated cellular

160 growth rates resulting in a complete abrogation of response in TCM even after 48 hours of

161 observation **(Fig. 2a,b, Fig. S2d, Movie 10)**. The same temperature increase in CACM, which

162 has reduced growth rates, resulted in a partial QS onset (88 out of 144 chambers assayed) that

163 was delayed by approximately 15-20 hours, matching the mathematical model predictions **(Fig.**

164 **S2e, Movie 11)**. To directly test whether protein abundance could modulate the onset of the QS

165 response, we transformed the cells with a construct coding for IPTG-inducible *LuxR* expression

166 **(Fig. S4c)**, and used it to examine the effect of LuxR overexpression on QS induced in TCM at

167 30°C. Overexpression of LuxR resulted in the rescue and immediate onset of QS response in all

168 chambers even at the elevated temperature **(Fig. 2c, Fig. S2f, Movie 12)**. As expected, the timing

169 of the onset of signaling was also dramatically shortened with overexpression of LuxR in TCM

170 at 25°C, with responses in all chambers triggered virtually immediately **(Fig. S2g, Movie 13)**.

171 Alternatively, if the level of glucose used for cell culture prior to the switch to TCM was lowered

8

172   (20 to 10 mM), which was expected to increase the basal level of LuxR expression due to both

173   partial catabolic de-repression and reduced cell growth, a decrease in the QS onset timing and

174   increase in the amplitude was observed **(Fig. S2h, Movie 14)**. Although these experiments

175   suggested the importance of achieving a high level of LuxR expression for QS onset, the onset

176   time was also dramatically decreased if exogenous AI was added at the time of the QS induction

177   in TCM and CACM at 25°C **(Fig. S2b, c)**. This result implied that QS onset can be accelerated if

178   the abundance of either LuxR or LuxI (and thus AI) is increased in the cells, which can be

179   controlled by the balance of synthesis and dilution of these proteins, as dictated by growth

180   conditions. On the other hand, consistent with the results above, the response magnitude, unlike

181   the response dynamics, was insensitive to exogenous AI (**Fig. 1i, Fig. S4d**), implying that AI,

182   under these conditions primarily controls the dynamics of the QS responses (Fig 2d). All of these

183   results were also well approximated by the corresponding versions of the mathematical model,

184   further supporting the PSD mechanism **(Fig. S2, 6)**.

185

186   Diverse conditions used in the experiments suggested that the QS outcome can be encoded not

187   only in the magnitude but also in the timing of the onset and the initial rate of the QS response

188   **(Fig. 2a, d, Fig. S6)**. This dynamic information can inform downstream responses long before

189   the steady state QS response is achieved. It is thus of interest to explore the sensitivity of the

190   dynamic aspects of QS to the various environmental conditions and to the degree of coupling

191   between the colony and the environment. One way to assay the sensitivity to environmental

192   inputs is an information theoretic approach[35,36], which, given the response variability, can

193   indicate how many input types or doses can be accurately resolved. Using this approach, we

194   found that the onset time showed the highest sensitivity in discriminating external environmental

9

195   conditions explored here, yielding 1.76 ± 0.03 bits of information, equivalent to accurately

196   distinguishing $2^{1.76} = 3.4$, or approximately 3 different types of conditions **(Fig. 2d, e, Fig. S7)**.

197   This discrimination capacity was in spite of the variability of environmental coupling across the

198   chambers, suggesting that the timing of the QS onset can provide the early information about the

199   changes in the environment regardless of the exact nature of the coupling of environment to the

200   cellular niche. Conversely, the response magnitude was the metric that was most sensitive to the

201   differential diffusive coupling, with at least 1 bit of information representing the ability to

202   accurately distinguish at least 2 coupling levels for each environmental condition **(Fig. 2d, f, Fig.**

203   **S8)**. The onset timing, on the other hand, was the least informative about this aspect of the cell

204   environment, consistent with the results above. This result suggested that the degree of cellular

205   confinement in a particular niche can indeed be conveyed by QS, but information about this

206   aspect of cell environment does not become available until high levels of response are attained.

207

208   We noted that our calculation of the information about the environmental coupling was likely an

209   underestimation, since the biphasic nature of the QS response distributions meant that two

210   distinct mean colony growth rates could correspond to the same mean QS response magnitude,

211   creating an ambiguity that can reduce the information content in the QS response magnitude.

212   Therefore, relatively slow and relatively fast growth can potentially result in the same QS

213   response magnitude and trigger the same levels of downstream adaptive response, unless there is

214   an additional means to resolve this ambiguity, a possibility that we explored next.

215

216   **Spatial properties of environmentally regulated QS response**

10

217   We hypothesized that the ambiguity associated with the biphasic dependence of the mean QS

218   response on the degree of coupling (growth rate) could potentially be resolved, if two different

219   chambers yielding the same average QS response magnitude at different growth rates would

220   have distinct spatial distributions of the QS signal. In particular, consumption of the nutrients

221   diffusing into the chambers by multiple cells within the chambers can lead to gradients of

222   nutrient availability, and thus, corresponding gradients of the cellular growth rates. As a result,

223   each chamber can span a range of growth rates, with growth rates higher in the chamber regions

224   adjacent to the coupling channels due to proximity to the nutrient source. We thus hypothesized

225   that the range of growth rates within a chamber can result in the range of QS responses

226   corresponding to the biphasic distribution curve measured before **(Fig. 3a)**. Consequently, the

227   spatial gradients of QS response within a chamber would correspond to a segment of the biphasic

228   dependence curve, with the local inclination of the segment specifying the direction of the spatial

229   gradient **(Fig. 3b)**. The biphasic nature of the curve would, therefore, specify gradients of

230   opposite signs, according to the rising and falling parts of the biphasic curve. Since the two

231   values of growth rates corresponding to the same QS response can map to two parts of the

232   biphasic curve with the opposite slopes, the resulting gradients of QS responses would be

233   opposite, providing extra information that can resolve the ambiguity discussed above.

234

235   We indeed found that different chambers incubated in TCM at 25°C for 24 hours had distinct

236   spatial QS magnitude distributions, and that the spatial gradient directions were fully consistent

237   with the hypothesis above, and thus the PSD hypothesis **(Fig. 3b-d Fig. S9a)**. We further

238   explored if this hypothesis could also account for the dynamics of spatial QS response evolution.

239   In particular, we investigated if this spatial dynamics can be accounted for by the dynamics of

11

240   the mean QS responses **(Fig. S10, 11)**. For example, the QS response distribution is biphasic

241   throughout the 24 hours of QS induction in TCM at 25°C, implying that the location of

242   maximum QS response in chambers with lower average growth rates would be proximal to the

243   nutrient-supplying channels throughout the response, starting from onset **(Fig. 3c-e, Fig. S10,**

244   **11)**. On the other hand, the maximal response would occur in more distal regions for chambers

245   with higher average growth rates. Indeed, we found that the onset position for QS in both TCM

246   and CACM conditions corresponded to the location of the maximal response as well as the local

247   inclination of the biphasic curve, shifting from proximal to distal regions of the chamber when

248   examining chambers with increasing mean growth rates **(Fig. 3f, Fig. S9b, S12)**. Overall, these

249   results suggest that both the average QS response magnitude and the spatial gradients of the QS

250   response in individual chambers can be accounted for by the same mechanism. This observation

251   suggests that the biphasic nature of the response magnitude distribution, explained by the PSD

252   mechanism, can lead to a variety of spatial QS distributions, as a function of coupling between

253   the cellular niches and extracellular milieu.

254

255   **Temporal thresholds and bistability in QS response**

256   Our data suggests that the dynamics of QS response can convey the information on a persistent

257   change in the environmental conditions, particularly the nutrient content, with this information

258   further refined as a function of the degree of diffusive coupling, resulting in nonuniform spatial

259   distributions of the signaling magnitude. However, the changes in the environment are frequently

260   transient or display complex dynamics. We thus investigated how QS responds to such dynamic

261   conditions. In particular, we investigated if variable QS onset timing can translate into condition-

262   dependent temporal thresholding, requiring a persistent rather transient change in the

12

263   environment, longer than a certain threshold, for the response to occur **(Fig. 4a)**. We explored

264   this possibility by transiently switching from the glucose-rich TCM to the QS-inducing TCM at

265   25°C for 4 hours, which is shorter than the fastest onset timing of ~7 hours in these conditions

266   **(Fig. 1h)**. This transient change in the environment indeed resulted in no detectable QS response

267   in both simulations and experiments, suggesting a temporal filtering of inputs below a threshold

268   duration **(Fig. 4b, Fig. S13a, Movie 15)**. Furthermore, periodic changes in cell environment

269   between TCM and glucose-rich medium (4 hour-long pulses, 50% duty cycle) again resulted in

270   the absence of QS response, implying no temporal integration of the transient inputs **(Fig. S13b,**

271   **Movie 16)**. On the other hand, a 16-hour stimulation with the TCM, exceeding the slowest QS

272   onset time among cells, enabled the response in all chambers **(Fig. 4b, Fig. S13c, Movie 17)**.

273   This response recovered to the baseline in all but 3 chambers within 24 hours after restoring

274   glucose-rich conditions. In combination, these results suggested effective temporal filtering of

275   the environmental changes by the QS circuit, ensuring that only sufficiently persistent signals

276   activate the response.

277

278   The 3 chambers retaining the QS signaling following transient stimulation were the ones with the

279   slowest growth rates **(Fig. 4b, Fig. S14a)**. Since transient responses can be stabilized by the

280   positive feedback and the associated bistability and hysteresis, we hypothesized that the QS-

281   associated positive feedback might be maintaining the response in a subset of chambers, even in

282   the presence of the glucose-rich environmental conditions. Further analysis and our prior work[30]

283   suggest that the bistability regime, and thus, the number of chambers retaining the response

284   following transient stimulation, can be expanded by lowering glucose concentrations in the

285   medium prior to and following the transient stimulation **(Fig. 4c)**. Indeed, for cells pre-incubated

13

286   in 10 mM glucose (mean QS onset time of 7.5 ± 1.5 hours), glucose removal for 4 hours was

287   sufficient to elicit QS in several, but not all, chambers, again supporting the existence of a

288   temporal threshold, albeit lowered for this condition **(Fig. 4b, Fig. S13d, 14b, Movie 18)**.

289   Consistent with the previous results, the chambers showing the QS response in this experiment

290   were also the ones with slower growth rates and thus included those that displayed persistent

291   response after cessation of the stimulus. As hypothesized, the number of chambers where QS

292   was persistently retained after removal of the stimulus increased to 7. Extending the stimulus

293   duration to 9 hours permitted all chambers to become transiently induced and achieve higher

294   amplitudes of induction, but did not affect the number of chambers displaying irreversible QS

295   **(Fig. S13e, Movie 19)**. These results highlighted a strong bi-stable nature of the response

296   consistent with the positive feedback interactions within the *lux* signaling circuit[27,30] leading to a

297   'memory' of a prior induction even if the environmental conditions no longer favor QS. Overall,

298   we concluded that better environmental coupling and more nutritious environment can impart

299   longer temporal thresholds ensuring a low and transient QS response for a subset of chambers

300   exposed to a transient change in the environment **(Fig. 4c)**. On the other hand, poorer

301   environmental coupling and less nutritious environments can each reduce the temporal threshold

302   and ensure persistent QS responses in an increasing number of micro-chambers **(Fig. 4c).**

303

304   **Cell communication allows a small pre-induced cell sub-population to quicken the onset of**

305   **response in the rest of the population through cell communication**

306   Visual inspection of chambers with persistent QS response revealed that only small fractions of

307   cells were highly induced, with the rest of the population displaying no detectable QS signaling

308   **(Fig. S14, Movie 17-19)**. The higher-than-basal levels of AI produced by the induced

14

309   subpopulation could be key to the maintenance of the high stable state of expression of QS

310   genes[37,38] in the presence of active environmental suppression. Indeed, simultaneous induction

311   and repression with exogenous AI and glucose, respectively, stably maintained an induced

312   subpopulation **(Fig. S15, Movie 20)**. Furthermore, we hypothesized that this subset of cells could

313   carry a memory of a prior stimulation, which can provide a selective advantage if conditions

314   become adverse, and thus, stimulatory again. Although this strategy is superficially similar to the

315   commonly assumed 'hedging of bets' scenario[39,40], which postulates that a diversification of

316   response within a population can confer a selective advantage under uncertain environmental

317   conditions, the cell-cell communication nature of QS imparts additional benefits. In particular,

318   the induced cells can potentially promote induction of neighboring cells after worsening of

319   conditions through secretion of AI, thus quickening the timing of the QS onset in the uninduced

320   cells, permitting a greater fraction of cells to faster assume the required adaptive phenotype. We

321   thus explored if cell communication inherent to QS can indeed reduce the temporal threshold and

322   accelerate the onset of response.

323

324   To compare the temporal threshold between fully uninduced and partially induced cell

325   populations, we modified the microfluidic platform to screen distinct environmental conditions

326   that can yield such populations simultaneously. More specifically, we explored 12 chamber

327   configurations in the presence of several glucose concentrations in the 0-6 mM range **(Fig. 4d,**

328   **Fig. S16)**, which enabled us to elicit a wide spectrum of responses ranging from complete

329   presence to complete absence of induction within the chamber configuration with the highest

330   diffusive coupling **(Fig. S17a, Movie 21)**. We found that in the 0-0.86 mM range of glucose

331   concentrations, the cells in the colonies were fully induced, whereas in the 1.71-6 mM range, we

332   observed bi-stable responses, with chambers showing different fractions of induced cells that

333   were stably maintained for at least 40 hours after initial onset **(Fig. 4e, g, Movie 21).** In the cases

334   of 1.71 and 2.57 mM, the bi-stability resulted in either complete (ranging from $18.77\pm8.26\%$ to

335    $97.26\pm0.72\%$) or partial (ranging from $0.037\pm0.066\%$ to $12.19\pm6.82\%$) induction in different

336   chambers, while chambers in the 4.29-6 mM range contained either partially induced or

337   completely un-induced (ranging from $0.0015\pm0.0009\%$ to $0.0079\pm0.0047\%$) cell populations

338   **(Fig. S18)**. This range of distinct bi-stable responses allowed us to examine whether and how the

339   presence of different fractions of induced cells would affect the QS response **(Fig. 4f)**.

340

341   To accomplish this, we studied the effect of switching to TCM from all glucose supplemented

342   conditions, which resulted in a complete QS induction for all chambers, but with distinct onset

343   times **(Fig. 4h, Fig. S17b, Movie 22, 23).** In all cases, we compared, for the same glucose level,

344   the onset timing of uninduced cells either in the fully uninduced populations or populations

345   containing a fraction of induced cells, due to the underlying bi-stability. For all glucose levels,

346   we found that the presence of a fraction of induced cells dramatically shortened the QS onset

347   time in uninduced cells **(Fig. 4i, Fig. S19).** Notably, the most dramatic relative change in the

348   onset timing was observed between 3.43 and 4.29 mM of glucose in the pre-incubation medium,

349   also coinciding with the lowest glucose levels allowing bi-stable responses and thus presence of

350   induced sub-populations. This result was consistent with AI-mediated cell-to-cell communication

351   from the induced subset of cells, pre-conditioning the remaining uninduced cells in the

352   population and thus promoting a quicker QS induction following the onset of adverse conditions.

353   This was also consistent with the faster onset of QS in separate experiments whereby cells were

354   exposed to low doses of exogenous AI **(Fig. S20, Movie 24-26).** These experiments suggested

16

355   that if the fitness of the population is coupled to the QS onset, the presence of the persistently

356   induced sub-population can provide a selective advantage to the whole population by enabling a

357   faster response to a dynamic change in the colony environment.

358

359   **<u>Discussion</u>**

360   QS is one of the most ancient mechanisms of cell communication, and yet, its functional role

361   remains ambiguous. It has been proposed that, in addition to the widely accepted cell density

362   sensing function, QS can also serve to assess the diffusive transport properties of the

363   microenvironment. Our results provide a more complex view of this archetypal signaling

364   mechanism, demonstrating that QS signaling is also sensitive to dynamic changes of

365   environmental conditions such as nutrient composition and access. The observed QS responses

366   are best explained not only by the currently accepted view of QS as driven by positive feedbacks

367   inherent in most QS genetic circuits, including the *lux* operon explored here, but also by the

368   balance of protein synthesis and dilution modulated by the specific microenvironments that the

369   cells are exposed to. In combination, these regulatory mechanisms endow the QS response with

370   several new properties that can strongly affect the fitness of the cell population and the outcome

371   of the adaptive processes frequently coupled to the QS activation.

372

373   We found that a subtle change in the nutrient source, such as the degree of digestion of casein,

374   can strongly influence the balance of the rates of cell growth rate and protein synthesis,

375   translating into the dilution and synthesis of the QS-mediating gene products. In particular, a

376   higher degree of digestion translated into a substantial increase in protein synthesis rate

377   accompanied by a decrease in cell proliferation. The reciprocal balance between protein

17

378   synthesis and cell proliferation may reflect a more general strategy of allocation of limited

379   available resources to different intracellular processes[41,42]. Importantly, this balance can also be

380   influenced by inputs other than nutrients, including, as shown here, gene amplification or altered

381   temperature. The resulting complex regulation translates into non-monotonic responses of the

382   long term QS amplitude as a function of colony growth rate, which in turn translates into the

383   distinct distributions of the spatial QS responses, with the gradients of the response pointing

384   either toward or away from the nutrient source. This inherent non-monotonicity might also

385   explain complex differentiation patterns of *B. subtilis* into a state of competence[43], suggesting

386   similar regulation in a distinct underlying QS circuit.

387

388   Successful adaption may depend not only on mounting the responses that are adequate to the

389   environmental challenges, but also on how quickly these responses can be mounted. The

390   bistability inherent in the positive feedback regulation of most known genetic QS circuits, when

391   modulated by the environmentally defined variable balance between growth rate and protein

392   synthesis, allows for complex decision-making. In particular, this regulatory mechanism can

393   ignore pulsatile environmental inputs, such as changes in nutrient content, that are too transient,

394   while responding to more persistent stimuli by either transient or persistent activation, lasting

395   long past the input cessation. The balance between protein synthesis and dilution is crucial for

396   establishing the time it takes to reach the critical concentrations of the regulatory proteins

397   enabling the QS response, and thus for controlling the temporal thresholding of inputs and the

398   timing of response initiation. This sensitivity of the initial response dynamics to the temporal

399   fluctuations of the extracellular milieu can supply the information on environmental changes to

18

400   the downstream, adaptive circuits far in advance of reaching the steady state of the QS response,

401   which may provide additional time for eliciting appropriate responses.

402

403   Similar considerations pertain to the cases of QS involvement in symbiotic settings, as for *V.*

404   *fischeri*, where the circadian cycles of animal foraging are synchronized with cycles of growth

405   and QS response by the symbiont bacterial cells. We find that amino acid-based nutrient sources,

406   thought to be the means of the host's support of *V. fischeri* growth *in vivo,* may support QS

407   response only in a certain range of temperatures, likely present in the context of ocean animals,

408   and with highly adjustable onset time, allowing the response to be regulated by nutrients not only

409   through control of cell density, but also more directly.

410

411   Our results also reveal a new aspect of the possible meaning of the messages exchanged by cells

412   during QS-related cell-communication. The persistent responses of cell sub-populations

413   following transient changes in the cell environment can serve as a type of memory of the recent

414   exposure to conditions promoting QS, even if the environment has since become benign. This

415   memory is carried not by the population as a whole but by different fractions of cells within the

416   population, which can be quite limited. As mentioned above, this strategy of diversification of

417   QS responses within a population may resemble the often discussed bet-hedging response, in

418   which a sub-population of cells may be more adapted to a possible change in the environment

419   than the rest of the population. However, in the case of the QS response, the non-autonomous

420   nature imparted by cell-cell coupling through secreted AI can allow the induced subpopulation,

421   which can anticipate the environmental change, to accelerate response by the uninduced cells, if

422   the conditions indeed change for the worse. This allows the uninduced cells to avoid the

19

423   metabolic costs associated with the initial QS induction but still enable faster onset of QS-

424   associated adaptive response when needed. In a sense, this represents a type of 'education' of

425   uninduced cells by the induced ones, providing the intercellular communication messages with a

426   specific meaning. The resulting higher overall population responsiveness can increase the

427   population fitness vs. the populations devoid of such cell 'education' capabilities.

428

429   **Methods**

430   **Design and fabrication of microfluidic device**

431   The overall organization of the channels and chambers in the microfluidic device is similar to

432   that in previous studies[44,45]. Briefly, an array of 16 parallel flow-through channels with a depth of

433   15 μm are connected to 24 rows of 30 chambers each, which house the cells. The dimensions of

434   the chambers are 100 x 100 x 0.8 μm, with a 15 x 15 μm post in the center. The degree to which

435   the chambers are connected to the flow-through channels via coupling channels are varied. 16

436   rows of chambers are connected to flow-through channels by coupling channels only on one

437   single side of the chamber, while eight rows of chambers are connected to flow-through channels

438   by coupling channels on two, opposing sides of the chamber. Each side of the chamber that is

439   connected to the flow-through channels has either one, two, or three coupling channels, giving

440   one-sided chambers a total of one, two, or three coupling channels, while double-sided chambers

441   have a total of two, four, or six coupling channels. In addition, the coupling channel dimensions

442   are 25 or 50 μm in length, and 10 or 20 μm in width. The combination of different dimensions

443   and configurations of coupling channels produced 24 unique chamber types with varying degrees

444   of mass transport properties. The chambers are organized into four quadrants of six types each,

445   with three single-sided and three double-sided chambers in each quadrant. Each group is then

20

446   distributed in a tandem, repeated triplet fashion, to ensure that each chamber type is distributed

447   evenly throughout the quadrant to minimize the effect of positional dependence relative to the

448   source of medium.

449

450   Growth medium is supplied from either one of two inlets, which connect to the flow-through

451   channels and supply nutrients to chambers on its way to a single outlet port, while the fluid from

452   the alternate inlet is directed to a waste port. Because the height of the chambers are relatively

453   shallow compared to the height of the flow-through channels, the chambers are much more

454   resistant to flow across the chamber as compared to flow through the channels, hence, the

455   dominant mode of mass transport into the chamber is through diffusion. The symmetric binary

456   branching of the flow-through channels ensures that the pressures are balanced between

457   channels, further preventing crossflow into the chamber. Flow is driven through the device via

458   hydrostatic pressure differences, with the height of the syringe connected to the inlet with the

459   desired medium higher than the alternate inlet, which are both higher than the syringes connected

460   to the outlet and waste port. The medium being supplied to the chambers from one inlet can be

461   instantaneously switched to that of the alternate inlet by swapping the height of the syringes,

462   allowing for rapid changes in the medium conditions.

463

464   A chemical gradient-generating microfluidic device was also used in this study, based off of the

465   Christmas tree design[46]. Similar to the device mentioned above, the gradient device contains 2

466   inlets, 1 outlet, and 1 waste port, allowing for similar operation under normal conditions.

467   However, between the chambers and the inlets are a series of serpentine channels, which can

468   perform mixing of solutions if medium from both inlets are supplied simultaneously. If one inlet

21

469   (source) contains a molecule which the other inlet (sink) lacks, each stage of serpentine channels

470   performs progressively more refined dilutions, resulting an increasingly resolved concentration

471   gradient spanning the two concentrations of the inlets. Individual concentration doses are

472   separated into channels, allowing downstream chambers to be exposed to different

473   concentrations. The device creates 8 linearly graded concentration doses from 2 input

474   concentrations, each connected to a row of 30 (only double-sided) or 90 (single- and double-

475   sided) chambers, depending on the design. The design with 30 chambers in each row has only a

476   chamber type with the highest degree of connectivity, while the design with 90 chambers in each

477   row has 12 chamber types, all of which are contain 25 μm long coupling channels. The heights

478   of the chamber and channels are the same as the device above, except the design with 90

479   chambers in each row have chamber heights of ~0.75 μm. The channels converge into the outlet

480   via the same symmetric binary branching structure, allowing for equal pressures. When a

481   gradient is desired, it can be generated by equating the pressure from both syringes and

482   supplying medium from both inlets at the same time. A fluorescent dye is used to visualize the

483   gradient.

484

485   The device was fabricated in a similar fashion as in previous studies[44,45]. Briefly, the initial

486   design was drawn in Adobe Illustrator and sent to be printed as a photomask. The photomask

487   was used to produce a master mold via photolithography. The master mold was made with a 3"

488   silicon wafer with a two-level micro-relief (0.8 μm and 15 μm) of a UV-curable epoxy (SU-8 by

489   MicroChem, Newton, MA). The first level was made with SU-8 2002 spun onto the silicon wafer

490   at an initial 500 rpm for 10 seconds with an acceleration index of 1, then 10000 rpm for 30

491   seconds with an acceleration index of 100, to produce a ~0.8 μm thick film. The chambers were

22

492   patterned with photolithography, followed by subsequent baking and development to form the

493   structures. The subsequent level was made with SU-8 2015 spun onto the silicon wafer at an

494   initial 500 rpm for 10 seconds with an acceleration index of 1, then 3250 rpm for 30 seconds

495   with an acceleration index of 2 to produce a ~15 μm thick film. The channels were patterned and

496   made as above. Microfluidic devices were then fabricated with PDMS (Sylgard 184, Dow

497   Corning) via soft lithography. A 5 mm thick cast of PDMS made with 10:1 ratio of elastomer

498   base to elastomer curing agent. The PDMS cast was peeled off the wafer and cut into individual

499   chips, and ports were punched with a 20 gauge luer stub. Devices were washed and hermetically

500   sealed to #1.5 microscope cover slips, then baked in a 130°C oven overnight prior to use.

501

502   **Strain and growth conditions**

503   MG1655 *E. coli* expressing a truncated Lux quorum sensing operon from *V. fischeri* made in a

504   previous study[30] was used. Briefly, MG01S, containing *luxR* divergently transcribed from P*luxI*

505   fused to *GFP*, and MG02S, which is identical to MG01S bar the addition of *LuxI* upstream of

506   *GFP* and under the same promoter, were made by the restriction digests of *Eco*RI-*Kpn*I and

507   *Eco*RI-*Bam*HI fragments of the lux operon from pLVA01 and pLVA02, respectively, and cloned

508   into pPROBE'-GFP-Tagless. An *Eco*RI-*Not*I digestion of the resulting plasmid and subsequent

509   cloning into λInCh vector allowed for the genomic integration of the lux quorum sensing circuit

510   into the *E. coli* MG1655 chromosome. 100 ug/mL ampicillin was added for selection.

511

512   The inducible LuxR strain was made by PCR amplification of the *LuxR* gene from MG02S with

513   forward primer 5' –

514   ATCTCTGAATTCCCGTTTTAATGATATATAACACGCAAAACTTGCGAC – 3', which

515   adds an *Eco*RI restriction site upstream of the *LuxR*, and reverse primer 5' –

516   CAAGTATGGTACCCGTACTTAACTTTTAAAGTATGGGCAATCAATTGCTCC – 3',

517   which adds a *Kpn*I restriction site downstream of the gene. The PCR fragment was cloned into

518   pEXT22 plasmid by digesting both with *Eco*RI and *Kpn*I, placing *LuxR* under the control of a tac

519   promoter. The subsequent plasmid was transformed into MG02S. LuxR overexpression was

520   induced with 1 mM IPTG added to growth medium. 50 ug/mL kanamycin was added for

521   selection.

522

523   Prior to every experiment, a single colony was selected from a plate and inoculated into LB with

524   the appropriate antibiotics and grown overnight at 30°C with shaking at 230 rpm. The next day,

525   the overnight culture was diluted 1:100 into CACM (2% casamino acids, 1x M9 salts (12.8g

526   Na_2HPO_4 $7H_2O$, 3g KH_2PO_4, 0.5g NaCl and 1g NH_4Cl per liter), 1 mM $MgCl_2$) with 20 mM

527   Succinate, 20 mM Glucose and 100 ug/mL ampicillin, and grown at 30°C with shaking at 230

528   RPM until the culture reached an OD_{600} of 0.2-0.3 (approximately 3-4 hours). The culture was

529   subsequently centrifuged and cell pellet re-suspended in 1% BSA in PBS prior to loading into

530   the device. Cell loading was performed from the outlet port of a BSA in PBS-primed device.

531   After loading into the device, growth medium with the appropriate antibiotics and 20 mM

532   glucose is supplied to the cells continuously via one or two inlets and the cells are grown at 30°C

533   until all chambers are full before beginning any experiment, unless otherwise indicated. Other

534   growth media used were all variations of the CACM, with 20 mM, 10 mM, or absence of

535   glucose, or the substitution of 2% casamino acids with 2% tryptone, both of which are sourced

536   from digestions of casein.

537

24

538 **Microscopy**

539 Widefield image acquisition was performed on a Nikon Eclipse TE2000 epifluorescence inverted

540 microscope equipped with a motorized stage (Prior Scientific, Cambridge, UK) and a Cascade

541 1K EMCCD camera (Photometrics, Tucson, Arizona). Timelapse images were acquired with a

542 Nikon Plan Fluor 40x/0.75 Ph2 DLL objective, while montage images were captured with a

543 Nikon Plan Fluor 10x/0.3 Ph1 DL objective, and stitched together automatically with 10% image

544 overlap with a custom MATLAB script. Both phase contrast and fluorescence images were

545 captured for timelapse and montage images. Timelapse images were acquired every 20 minutes,

546 with an exposure time of 100-500 ms, while the montage images were taken with an exposure

547 time of 1000ms. The excitation filter wavelengths used for GFP detection was 450-490nm

548 (Chroma, Rockingham, VT), while the emission filter wavelengths was 525nm. The excitation

549 filter wavelengths used for detection of Alexafluor 555 was 541 – 565 nm, while the emission

550 filter wavelengths was 584 – 679 nm. A spectral 2D template autofocus algorithm was used to

551 maintain the focus for the entire duration of timelapse imaging. For time-lapsed images, at least

552 two positions for each condition/chamber type was chosen for each experiment, while montages

553 varied from 42 to 77 images depending on the device used. Control of the microscope and

554 capture of images were performed in an automated fashion via Slidebook 5.5 (Intelligent

555 Imaging Innovations, Denver, Colorado).

556

557 Z-stacks were acquired with a Leica SP8 Laser Scanning Confocal microscope equipped with a

558 white light pulsed laser with continuous wavelength and hybrid detectors. Images were acquired

559 on a HC PL APO 40x/1.30 Oil, CS2 objective and the Leica Application Suite X software.

560

25

561 **Evaluation of transport and growth in microfluidic device**

562 The transport properties of the various chamber types were evaluated with a dye, which served as

563 a proxy for a diffusible molecule and allowed for the visualization of the diffusion process.

564 Alexa Fluor 555 Hydrazide (Thermo Fisher Scientific, Waltham, MA) was chosen as the dye due

565 to its relatively high molecular weight as compared to most diffusible molecules of interest

566 (1150, vs 213.23g/mol for AI and 180.16g/mol for glucose), giving it a smaller diffusion

567 coefficient and longer diffusion time. Thus, it served as a good representation of the dynamics of

568 even the slowest diffusing molecules while also accounting for the dynamics of a wide range of

569 molecules with faster diffusion dynamics. Cells were grown in dye-free medium within the

570 chambers overnight until the chambers were filled to capacity. 0.01 mM of dye solution was

571 perfused into the flow-through channels by increasing the hydrostatic pressure of the dye-

572 containing medium syringe relative to the dye-free medium syringe. Fluorescence timelapse

573 microscopy was used to capture the fluorescence intensity within the chambers, at a rate of 1

574 minute per time point, for a duration of 15 minutes. The diffusion of the dye out of the chamber

575 was also monitored by switching back to the dye-free medium syringe. The intensity of the

576 fluorescence in the chamber is quantified by taking the mean of the intensity of the entire

577 chamber for each time point, and normalized to the initial or final timepoint, for diffusion out

578 and diffusion in, respectively. The transport properties of the various chamber types was also

579 modeled computationally with COMSOL Multiphysics 4.2 (COMSOL Inc. Stockholm,

580 Sweden), the results of which was in agreement with experiments.

581

582 The growth rate of the cells within the different chambers was assessed with the MG01S strain,

583 which lacks the ability to produce LuxI. Therefore, the production of high levels of GFP relies on

26

584　the addition of exogenous AI, and ceases upon its removal. MG01S is loaded into chambers and

585　grown in the presence of 1 μM AI to induce uniform GFP production until all chambers are filled

586　to capacity. Once AI is removed, fluorescence in the chamber is gradually lost as the continual

587　growth of the cells within the chamber would lead to the distribution of a fixed number of GFP

588　protein to the progeny, which are gradually pushed out of the chamber by the growing and

589　dividing cells within the chamber and carried away by the flow. Due to the stability of the GFP

590　used[47], the loss of GFP fluorescence is expected to be predominantly from dilution of the protein

591　as a result of growth and division of the cells, the rate of which would be proportional to the

592　growth rate within different chambers. The average fluorescence over time can be fitted with an

593　exponential curve of the form a*exp(bt), giving an estimate of the growth rate. The growth rate

594　was estimated for all 24 chamber types with both casamino acids and tryptone-based minimal

595　media, and at 25 and 30°C.

596

597　**Image processing and data analysis**

598　Automated image acquisition was performed with Slidebook 5.5. Raw images were exported in

599　.tiff format and processed using custom MATLAB scripts. All images were corrected for uneven

600　illumination with the following correction: $C = (I-D)/(F-D)*M$, where C is the corrected image, I

601　is the initial image, D is the darkfield image, F is the flatfield image, and M is the mean of the

602　flatfield minus darkfield images. The flatfield and darkfield were averages of multiple images.

603　Time-lapse images were aligned automatically with an alignment algorithm, while montage

604　images were stitched together with the same alignment algorithm with 10% overlap between

605　adjacent images. Each calculated metric is an average of at least 3 independent experiments of at

606　least 2 replicates each for each chamber configuration, unless otherwise indicated.

27

607

608   The automated data analysis pipeline imports the processed image file and determines the square

609   chamber region, excluding the post, containing cells. The mean intensity value for the entire

610   chamber was determined for both sets of image types. For time-lapse images, this is done for all

611   time points, and additional metrics were also calculated. To visualize the spatial distribution of

612   response along the y-axis, the intensity values were averaged along the x-axis and the resultant

613   column of intensity values were normalized by subtracting the minimum and dividing by the

614   minimum-subtracted maximum. The steepness of spatial gradients at each time point was

615   approximated with the slope from a linear regression performed on the column of intensity

616   values versus a normalized distance of 1, with a positive slope representative of higher responses

617   in the distal regions relative to the coupling channels, and a negative slope representative of

618   higher responses in the proximal regions relative to the coupling channels. Double-sided

619   chambers are analyzed as half-chambers along the y-axis due to symmetry, and the calculated

620   metric for both halves are averaged into a single value to represent the whole chamber.

621   Aggregating these intensity value columns for each time point generated the kymographs used

622   for spatial analysis. Onset time is defined as the time point at which more than 1.5% of the pixels

623   within the square region of the chamber have intensity values greater than mean + 4*SD of the

624   same region in the initial frame. Onset location was quantified from the kymographs. Briefly, the

625   columns of normalized intensity values from the onset time point to a time point 2 hours later

626   were extracted, and the positions with a normalized value of greater than or equal to 0.99 were

627   collected and the mean and standard deviations were calculated. The initial rate was estimated

628   with the slope from a linear regression on the first 5 hours of response after the onset time within

629   exogenous induction conditions, which is expected to reach maximal levels of production. Time-

28

630   lapse fluorescence intensity measurements are normalized to the initial value. Two chamber

631   configurations were excluded (filled shapes) from the chip-wide measurements obtained from

632   the montage image analysis due to partial formation of cell bilayer, but z-sections from confocal

633   microscopy confirm the biphasic nature (Fig. S3). Fractions of induction within a chamber were

634   determined by the fraction of total pixels that exceeded a predetermined threshold value. For

635   categorization, mean±SD ≤10% and ≥0.01% were considered partially induced, less than that is

636   uninduced, and greater than that is fully induced. For chambers that are not packed at the

637   beginning of the experiment, segmentation of cells based on phase contrast images were

638   performed, and all quantified data from these chambers were from the segmented images.

639

640   Z-stacks from confocal microscopy were split into individual focal planes, with the chamber

641   region for each plane segmented and the mean intensity calculated. The slice with the highest

642   mean intensity was used for analysis, and were compared to the mean value from the maximum

643   intensity projections.

644

645   **Computation of mutual information**

646   Briefly, mutual information (I) between two random variables is calculated from the formula:

647    $$I(R; S) = H(R) - H(R|S), \qquad (1)$$

648   where S and R denote the signal and response, respectively, and H is the entropy function:

649    $$H(X) = -\sum_{i}^{n} p(x_i) log_2 p(x_i). \qquad (2)$$

650   Hence, formula (1) becomes:

29

651 $$I(R;S) = \sum_j -P(R = r_j)log_2 P(R = r_j)$$

652 $$-\sum_i P(S = s_i)\left(\sum_j -P(R = r_j|S = s_i)log_2 P(R = r_j|S = s_i)\right). \quad (3)$$

653 The marginal distribution of the response is

654 $$P(R = r_j) = \sum_i P(S = s_i)P(R = r_j|S = s_i). \qquad (4)$$

655 Since the formulas as shown above are for discrete data, the experimental data used for the

656 calculations, which lies on a continuous spectrum, are discretized by binning. However, binning

657 of the finite data sample results in biased estimates of the mutual information. Since bias is a

658 function of sample size, which approaches zero as sample size approaches infinity, we utilized

659 the series expansion of mutual information in terms of inverse sample size to estimate the

660 unbiased mutual information:

661 $$I_{biased} = I_\infty + \frac{a_1}{N} + \frac{a_2}{N^2} + \cdots. \qquad (5)$$

662 Here, I_{biased} is the biased estimate of mutual information, I_∞ is the unbiased estimate of mutual

663 information with infinite sample size, N is the total number of samples, and a_i are coefficients

664 dependent on the signal and response distributions. For sufficiently large N, all terms larger than

665 first order are negligible, resulting in the biased estimate of mutual information being a linear

666 function of inverse sample size. As a result, we can use jackknife sampling to sample subsets of

667 the data to compute the mutual information. By plotting these biased estimates of mutual

668 information to the inverse sample size, fitting a line, and extrapolating to infinite sample size, we

30

669   can obtain the unbiased estimate of mutual information. For a more comprehensive description,

670   we refer the reader to previously published work[35,36].

671

672   **Model and simulations**

673   ***Simulation of diffusion***

674   Diffusion dynamics were simulated using COMSOL Multiphysics 4.2. Briefly, the 3D geometry

675   of each chamber configuration was recreated within the software, and the concentration of the

676   entire volume of the chamber was set to an initial concentration of 0 mM. All surfaces of the

677   chamber were set to have null flux except for the surfaces that interface with the flow-through

678   channels, which are set to a constant concentration of 0.01 mM, corresponding to the

679   concentration of dye used in the experiment. A diffusion coefficient of $2 \times 10^{-10}\ m^2\ s^{-1}$ was

680   used for the Alexa Fluor 555 dye. Time-dependent transport of diluted species simulations were

681   performed for all 24 chamber configurations. The average concentration within the chamber

682   volume was determined and plotted.

683

684   ***Simulation of QS response***

685   The mathematical model is a simplified version of a model from a previous study[34], accounting

686   for only one cell, but with new species and terms added:

$$\frac{d[R]}{dt} = k_6 + \frac{k_3[C]}{K_{DR}+[C]} - k_{10}[R] - k_1[R][A] + k_{-1}[RA] - k_{11}[R] \qquad (6)$$

$$\frac{d[RA]}{dt} = k_1[R][A] - k_{-1}[RA] - 2k_2[RA]^2 + 2k_{-2}[C] - k_{11}[RA] \qquad (7)$$

$$\frac{d[C]}{dt} = k_2[RA]^2 - k_{-2}[C] - k_{11}[C] \qquad (8)$$

31

690 $$\frac{d[I]}{dt} = k_7 + \frac{k_4[C]}{K_{DI}+[C]} - k_{11}[I] - k_8[I] \tag{9}$$

691 $$\frac{d[G]}{dt} = k_7 + \frac{k_4[C]}{K_{DI}+[C]} - k_{11}[G] - k_9[G] \tag{10}$$

692 $$\frac{d[A]}{dt} = -k_1[R][A] + k_{-1}[RA] - k_{-13}[A] + k_{13}[A_e] + k_5[I] \tag{11}$$

693 $$\frac{d[A_e]}{dt} = k_{-13}[A] - k_{13}[A_e] - k_{12}[A_e] \tag{12}$$

694   Diffusion of AI is only considered as a rate of loss from the cell, if no exogenous AI is

695   introduced. In addition, the production of AI from C has been explicitly separated into

696   production of LuxI from C (which then produces AI) to enable the account of LuxI dilution.

697   Because GFP is downstream of LuxI, the added equation is nearly identical, with a different

698   degradation term the only difference. Dilution terms were also added to the equations of all

699   protein species to account for loss of protein from cell division.

700

701   The global constants that are applicable to all the conditions are listed in Table 1, most of which

702   were based on a previous study[33]. For each environmental condition, a new set of k_4 (synthesis,

703   Table 2) and k_{11} (dilution, Table 3) values were used, the range of which corresponds to the

704   different chamber configurations, and were measured from experiments. k_4 (synthesis) was

705   estimated with the slope from a linear regression corresponding to the first 5 hours of response

706   after the onset time within exogenous induction conditions, which is expected to reach maximal

707   levels of production. Dilution rates are proportional to growth rate, so k_{11} (dilution) is calculated

708   in the same way with an exponential fit of the GFP dilution data. The exceptions are k_4

709   (synthesis) for tryptone and casamino acids conditions at 30°C, which were inferred by

710   comparing the change in growth rates and synthesis rates from tryptone to casamino acids

32

711   medium at 25°C, and extrapolating that relationship to the change in temperature from 25°C to

712   30°C in both media types.

713

714   Simulations were performed in MATLAB. Briefly, each simulation was run for an initial 24

715   simulation hours with either the LuxR repressed or LuxR partially repressed k_3 and k_6 values, to

716   replicate the initial growth in 20 mM or 10 mM glucose medium, respectively, and to allow for a

717   basal steady state amount of proteins and components to be made. The k_3 and k_6 values are

718   subsequently switched to the derepressed or overexpressed form, and simulation resumed for at

719   least another 24 simulation hours. Simulations corresponding to the transient glucose switching

720   experiments consisted of transient changes in the k_3 and k_6 values at the appropriate time points.

721

722   **Statistical Analysis**

723   At least 3 independent tests were performed for each experiment unless otherwise stated. F-test

724   was performed to determine variances between samples. 2-tailed t-tests were used for

725   comparisons.

726

727   **Code Availability**

728   The codes used in this study are available from the corresponding author upon request.

729

730   **Data Availability**

731   The data that support the findings of this study are available from the corresponding author upon

732   request.

733
734

735   1   Gestwicki, J. E. & Kiessling, L. L. Inter-receptor communication through arrays of
736   bacterial chemoreceptors. *Nature* **415**, 81-84, doi:10.1038/415081a (2002).
737   2   Ajon, M. *et al.* UV-inducible DNA exchange in hyperthermophilic archaea mediated by
738   type IV pili. *Mol Microbiol* **82**, 807-817, doi:10.1111/j.1365-2958.2011.07861.x (2011).
739   3   McLean, B. G., Hempel, F. D. & Zambryski, P. C. Plant intercellular communication via
740   plasmodesmata. *Plant Cell* **9**, 1043-1054, doi:10.1105/tpc.9.7.1043 (1997).
741   4   Puliafito, A. *et al.* Collective and single cell behavior in epithelial contact inhibition.
742   *Proc Natl Acad Sci U S A* **109**, 739-744, doi:10.1073/pnas.1007809109 (2012).
743   5   Popat, R., Cornforth, D. M., McNally, L. & Brown, S. P. Collective sensing and
744   collective responses in quorum-sensing bacteria. *J R Soc Interface* **12**,
745   doi:10.1098/rsif.2014.0882 (2015).
746   6   Miller, M. B. & Bassler, B. L. Quorum sensing in bacteria. *Annu Rev Microbiol* **55**, 165-
747   199, doi:10.1146/annurev.micro.55.1.165 (2001).
748   7   Ng, W. L. & Bassler, B. L. Bacterial quorum-sensing network architectures. *Annu Rev
749   Genet* **43**, 197-222, doi:10.1146/annurev-genet-102108-134304 (2009).
750   8   Shapiro, J. A. Thinking about bacterial populations as multicellular organisms. *Annu Rev
751   Microbiol* **52**, 81-104, doi:10.1146/annurev.micro.52.1.81 (1998).
752   9   Swift, S. *et al.* Quorum sensing as a population-density-dependent determinant of
753   bacterial physiology. *Adv Microb Physiol* **45**, 199-270 (2001).
754   10   Gao, M. *et al.* A crucial role for spatial distribution in bacterial quorum sensing. *Sci Rep*
755   **6**, 34695, doi:10.1038/srep34695 (2016).
756   11   Boedicker, J. Q., Vincent, M. E. & Ismagilov, R. F. Microfluidic confinement of single
757   cells of bacteria in small volumes initiates high-density behavior of quorum sensing and
758   growth and reveals its variability. *Angew Chem Int Ed Engl* **48**, 5908-5911,
759   doi:10.1002/anie.200901550 (2009).
760   12   Hense, B. A. *et al.* Does efficiency sensing unify diffusion and quorum sensing? *Nat Rev
761   Microbiol* **5**, 230-239, doi:10.1038/nrmicro1600 (2007).
762   13   Redfield, R. J. Is quorum sensing a side effect of diffusion sensing? *Trends Microbiol* **10**,
763   365-370 (2002).
764   14   Perchat, S. *et al.* How Quorum Sensing Connects Sporulation to Necrotrophism in
765   Bacillus thuringiensis. *PLoS Pathog* **12**, e1005779, doi:10.1371/journal.ppat.1005779
766   (2016).
767   15   Steiner, E., Scott, J., Minton, N. P. & Winzer, K. An agr quorum sensing system that
768   regulates granulose formation and sporulation in Clostridium acetobutylicum. *Appl
769   Environ Microbiol* **78**, 1113-1122, doi:10.1128/AEM.06376-11 (2012).
770   16   Antunes, L. C., Ferreira, R. B., Buckner, M. M. & Finlay, B. B. Quorum sensing in
771   bacterial virulence. *Microbiology* **156**, 2271-2282, doi:10.1099/mic.0.038794-0 (2010).
772   17   Rumbaugh, K. P. *et al.* Kin selection, quorum sensing and virulence in pathogenic
773   bacteria. *Proc Biol Sci* **279**, 3584-3588, doi:10.1098/rspb.2012.0843 (2012).
774   18   Zheng, J., Shin, O. S., Cameron, D. E. & Mekalanos, J. J. Quorum sensing and a global
775   regulator TsrA control expression of type VI secretion and virulence in Vibrio cholerae.
776   *Proc Natl Acad Sci U S A* **107**, 21128-21133, doi:10.1073/pnas.1014998107 (2010).
777   19   Bodelon, G. *et al.* Detection and imaging of quorum sensing in Pseudomonas aeruginosa
778   biofilm communities by surface-enhanced resonance Raman scattering. *Nat Mater* **15**,
779   1203-1211, doi:10.1038/nmat4720 (2016).

780 20   Kim, M. K. *et al.* Surface-attached molecules control Staphylococcus aureus quorum
781   sensing and biofilm development. *Nat Microbiol* **2**, 17080,
782   doi:10.1038/nmicrobiol.2017.80 (2017).
783 21   Parsek, M. R. & Greenberg, E. P. Sociomicrobiology: the connections between quorum
784   sensing and biofilms. *Trends Microbiol* **13**, 27-33, doi:10.1016/j.tim.2004.11.007 (2005).
785 22   Stewart, P. S. & Franklin, M. J. Physiological heterogeneity in biofilms. *Nat Rev*
786   *Microbiol* **6**, 199-210, doi:10.1038/nrmicro1838 (2008).
787 23   Moreno-Gamez, S. *et al.* Quorum sensing integrates environmental cues, cell density and
788   cell history to control bacterial competence. *Nat Commun* **8**, 854, doi:10.1038/s41467-
789   017-00903-y (2017).
790 24   Singh, P. K. *et al.* Vibrio cholerae Combines Individual and Collective Sensing to
791   Trigger Biofilm Dispersal. *Curr Biol* **27**, 3359-3366 e3357,
792   doi:10.1016/j.cub.2017.09.041 (2017).
793 25   Shadel, G. S. & Baldwin, T. O. Positive autoregulation of the Vibrio fischeri luxR gene.
794   LuxR and autoinducer activate cAMP-catabolite gene activator protein complex-
795   independent and -dependent luxR transcription. *J Biol Chem* **267**, 7696-7702 (1992).
796 26   Miyashiro, T. & Ruby, E. G. Shedding light on bioluminescence regulation in Vibrio
797   fischeri. *Mol Microbiol* **84**, 795-806, doi:10.1111/j.1365-2958.2012.08065.x (2012).
798 27   Shadel, G. S. & Baldwin, T. O. The Vibrio fischeri LuxR protein is capable of
799   bidirectional stimulation of transcription and both positive and negative regulation of the
800   luxR gene. *J Bacteriol* **173**, 568-574 (1991).
801 28   Stevens, A. M., Dolan, K. M. & Greenberg, E. P. Synergistic binding of the Vibrio
802   fischeri LuxR transcriptional activator domain and RNA polymerase to the lux promoter
803   region. *Proc Natl Acad Sci U S A* **91**, 12619-12623 (1994).
804 29   Haseltine, E. L. & Arnold, F. H. Implications of rewiring bacterial quorum sensing. *Appl*
805   *Environ Microbiol* **74**, 437-445, doi:10.1128/AEM.01688-07 (2008).
806 30   Williams, J. W., Cui, X., Levchenko, A. & Stevens, A. M. Robust and sensitive control
807   of a quorum-sensing circuit by two interlocked feedback loops. *Mol Syst Biol* **4**, 234,
808   doi:10.1038/msb.2008.70 (2008).
809 31   Gorke, B. & Stulke, J. Carbon catabolite repression in bacteria: many ways to make the
810   most out of nutrients. *Nat Rev Microbiol* **6**, 613-624, doi:10.1038/nrmicro1932 (2008).
811 32   Dunlap, P. V. & Greenberg, E. P. Control of Vibrio fischeri lux gene transcription by a
812   cyclic AMP receptor protein-luxR protein regulatory circuit. *J Bacteriol* **170**, 4040-4046
813   (1988).
814 33   Goryachev, A. B., Toh, D. J. & Lee, T. Systems analysis of a quorum sensing network:
815   design constraints imposed by the functional requirements, network topology and kinetic
816   constants. *Biosystems* **83**, 178-187, doi:10.1016/j.biosystems.2005.04.006 (2006).
817 34   Melke, P., Sahlin, P., Levchenko, A. & Jonsson, H. A cell-based model for quorum
818   sensing in heterogeneous bacterial colonies. *PLoS Comput Biol* **6**, e1000819,
819   doi:10.1371/journal.pcbi.1000819 (2010).
820 35   Cheong, R., Rhee, A., Wang, C. J., Nemenman, I. & Levchenko, A. Information
821   transduction capacity of noisy biochemical signaling networks. *Science* **334**, 354-358,
822   doi:10.1126/science.1204553 (2011).
823 36   Rhee, A., Cheong, R. & Levchenko, A. The application of information theory to
824   biochemical signaling systems. *Phys Biol* **9**, 045011, doi:10.1088/1478-3975/9/4/045011
825   (2012).

826 37 Bauer, M., Knebel, J., Lechner, M., Pickl, P. & Frey, E. Ecological feedback in quorum-
827   sensing microbial populations can induce heterogeneous production of autoinducers. *Elife*
828   **6**, doi:10.7554/eLife.25773 (2017).
829 38 Bareia, T., Pollak, S. & Eldar, A. Self-sensing in Bacillus subtilis quorum-sensing
830   systems. *Nat Microbiol* **3**, 83-89, doi:10.1038/s41564-017-0044-z (2018).
831 39 Beaumont, H. J., Gallie, J., Kost, C., Ferguson, G. C. & Rainey, P. B. Experimental
832   evolution of bet hedging. *Nature* **462**, 90-93, doi:10.1038/nature08504 (2009).
833 40 Solopova, A. *et al.* Bet-hedging during bacterial diauxic shift. *Proc Natl Acad Sci U S A*
834   **111**, 7427-7432, doi:10.1073/pnas.1320063111 (2014).
835 41 You, C. *et al.* Coordination of bacterial proteome with metabolism by cyclic AMP
836   signalling. *Nature* **500**, 301-306, doi:10.1038/nature12446 (2013).
837 42 Giordano, N., Mairet, F., Gouze, J. L., Geiselmann, J. & de Jong, H. Dynamical
838   Allocation of Cellular Resources as an Optimal Control Problem: Novel Insights into
839   Microbial Growth Strategies. *PLoS Comput Biol* **12**, e1004802,
840   doi:10.1371/journal.pcbi.1004802 (2016).
841 43 Ribbe, J. & Maier, B. Density-Dependent Differentiation of Bacteria in Spatially
842   Structured Open Systems. *Biophys J* **110**, 1648-1660, doi:10.1016/j.bpj.2016.03.007
843   (2016).
844 44 Groisman, A. *et al.* A microfluidic chemostat for experiments with bacterial and yeast
845   cells. *Nat Methods* **2**, 685-689, doi:10.1038/nmeth784 (2005).
846 45 Cho, H. *et al.* Self-organization in high-density bacterial colonies: efficient crowd
847   control. *PLoS Biol* **5**, e302, doi:10.1371/journal.pbio.0050302 (2007).
848 46 Dertinger, S. K. W., Chiu, D. T., Jeon, N. L. & Whitesides, G. M. Generation of
849   Gradients Having Complex Shapes Using Microfluidic Networks. *Analytical Chemistry*
850   **73**, 1240-1246, doi:10.1021/ac001132d (2001).
851 47 Miller, W. G., Leveau, J. H. & Lindow, S. E. Improved gfp and inaZ broad-host-range
852   promoter-probe vectors. *Mol Plant Microbe Interact* **13**, 1243-1250,
853   doi:10.1094/MPMI.2000.13.11.1243 (2000).
854

Acknowledgements

Author Contributions

859 E.K.C., A.G. and A.L. designed the device and E.K.C. fabricated the device. E.K.C. performed

860 experiments and simulations, and analyzed data. E.K.C. and A.L. wrote the paper.

Competing Interests

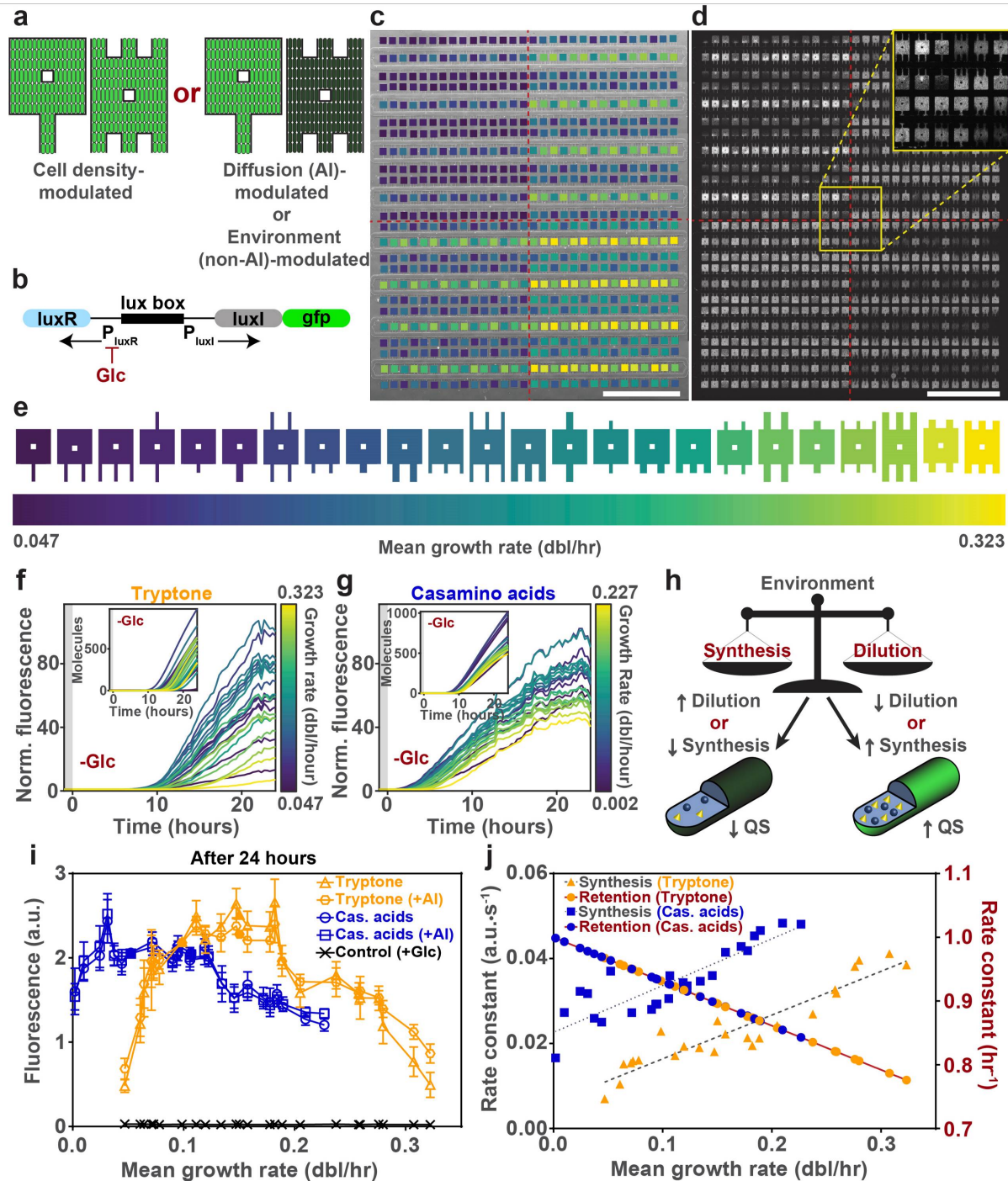862 The authors declare no competing interests.

Figure 1 QS is defined by a balance between nutrient-defined protein synthesis and dilution due to cell proliferation. a, QS is traditionally interpreted as either a mechanism for cell number/density sensing or diffusive environment sensing, which would lead to different response outcomes in certain environments. **b,** Diagram of QS circuit used in the study. **c,** Phase contrast

868 micrograph of microfluidic device chamber array overlaid with color-coding corresponding to

869 the 24 unique chamber configurations. Scale bar, 1 mm. **d**, Fluorescence micrograph of

870 microfluidic device chamber array taken 24 hours after auto-induced QS response in tryptone

871 medium at 25°C. Inset contain magnified view of the region indicated, which contains all 24

872 chamber configurations. Scale bar, 1 mm. **e**, Color-coding of chamber configurations based on

873 mean growth rate in tryptone medium. **f**, **g**, Auto-induction response dynamics over 24 hours in

874 tryptone **(f)** and casamino acids **(g)** media. (mean, n = 6, from 3 independent experiments). Insets

875 denote simulated dynamics obtained by varying only synthesis and dilution with parameters from

876 **(j)**. **h,** Proposed regulatory mechanism of QS response based on the balance of synthesis and

877 dilution of QS machinery proteins. **i**, Distributions of QS response magnitudes after 24 hours in

878 various nutrient and induction conditions. Filled shapes indicate the 2 chamber types excluded

879 from this analysis due to partial formation of cell bilayer (Supp. Info.) (n=105 or n=60, for

880 single- or double-sided chambers, respectively, from 3 independent experiments, mean ± SD). **j,**

881 Measured synthesis and dilution (growth) rate constants from tryptone and casamino acids media
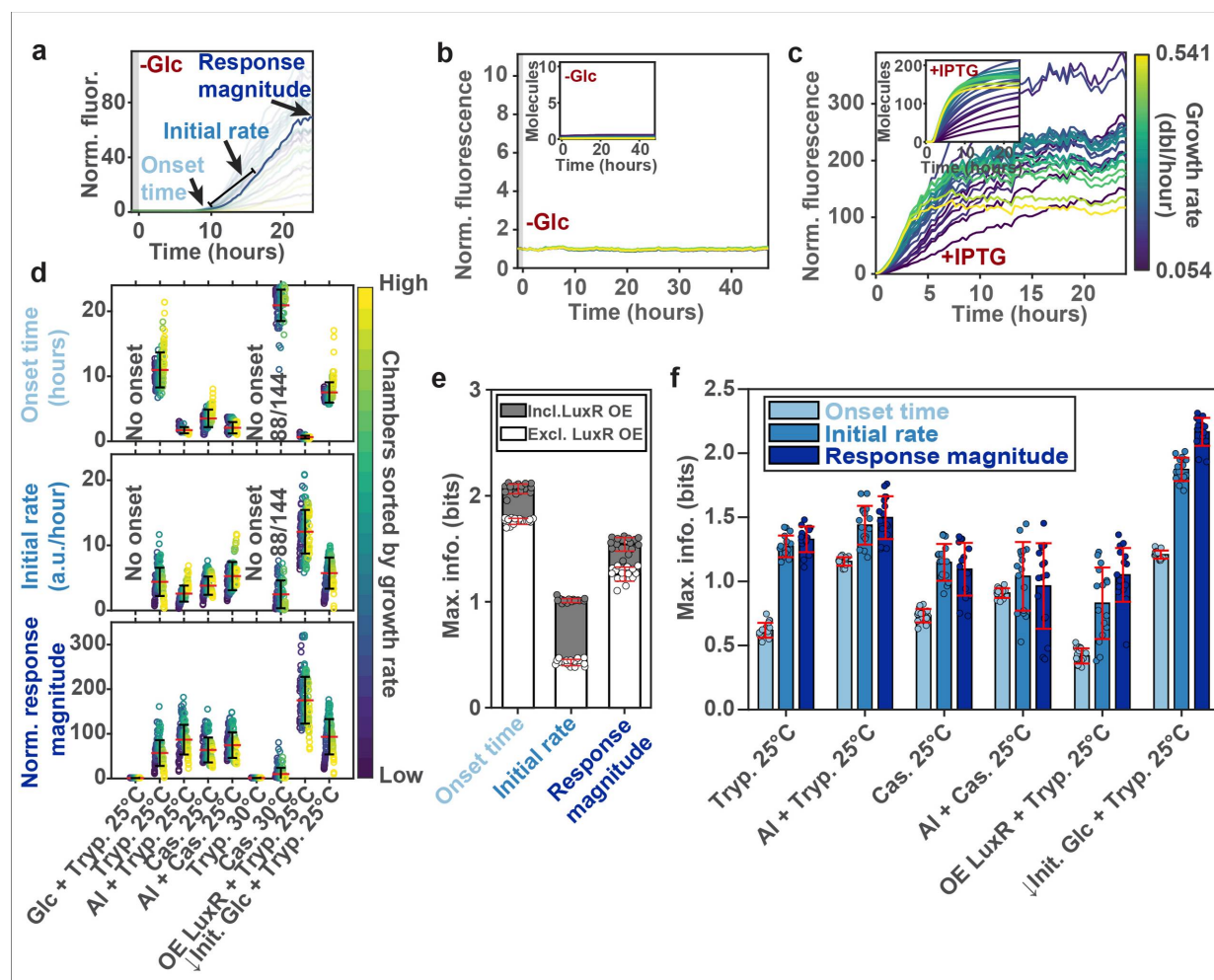
882 conditions.

883

884

Figure 2 Information about distinct environmental conditions is reflected in QS response

dynamics. a, Separation of QS dynamics into three components: onset time, initial response rate

and 24th hour response magnitude. **b,c,** Response dynamics within, **(b)** tryptone medium at 30°C,

and **(c)** tryptone medium with 1 mM IPTG (for LuxR overexpression) at 30°C (mean, n = 6,

from 3 independent experiments). Insets denote simulated dynamics. **d,** Summary of onset times,

initial rates, and response magnitudes from various conditions (n = 144, from 3 independent

experiments). **e**, Comparison of information about global environmental conditions discerned by

each component of QS dynamics assuming all chamber configurations are equivalent. **f,**

Comparison of information about the local differential coupling environment discerned by each

component of QS dynamics for various global environmental conditions. (mean ± SD)
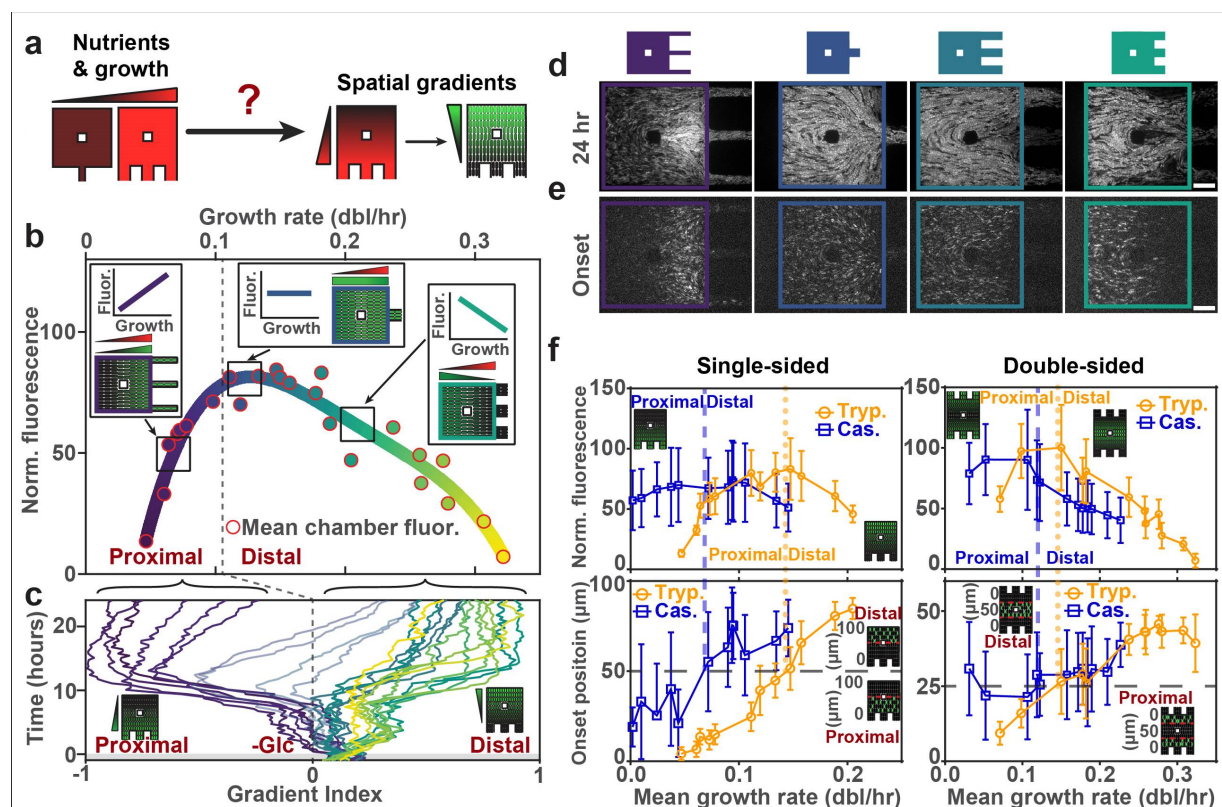
39

Figure 3 Spatial properties of environmentally regulated QS response dependence. a, Spatial dependence could arise from nutrient and growth gradients within the chamber. **b,** The proposed relationship between spatial response gradients and the biphasic response magnitude distribution. **c,** Quantification of auto-induction spatial response gradient dynamics over 24 hours in tryptone medium at 25°C. Positive gradient index indicates higher response in the regions distal from the coupling channels, whereas negative gradient index indicates higher response in the regions proximal from the coupling channels. (mean, n = 6, from 3 independent experiments). **d,e,** Fluorescence micrographs of chamber configurations corresponding to those illustrated in **(b),** at 24th hour **(d)** and at onset **(e)**. Scale bar, 20 μm. **f,** Spatial localization of auto-induced QS response onset in single- and double-sided chambers in tryptone and casamino acid media at 25°C, in relation to response magnitude distributions after 24 hours in the same conditions (n = 43-64, from 3 independent experiments) (mean ± SD).

40

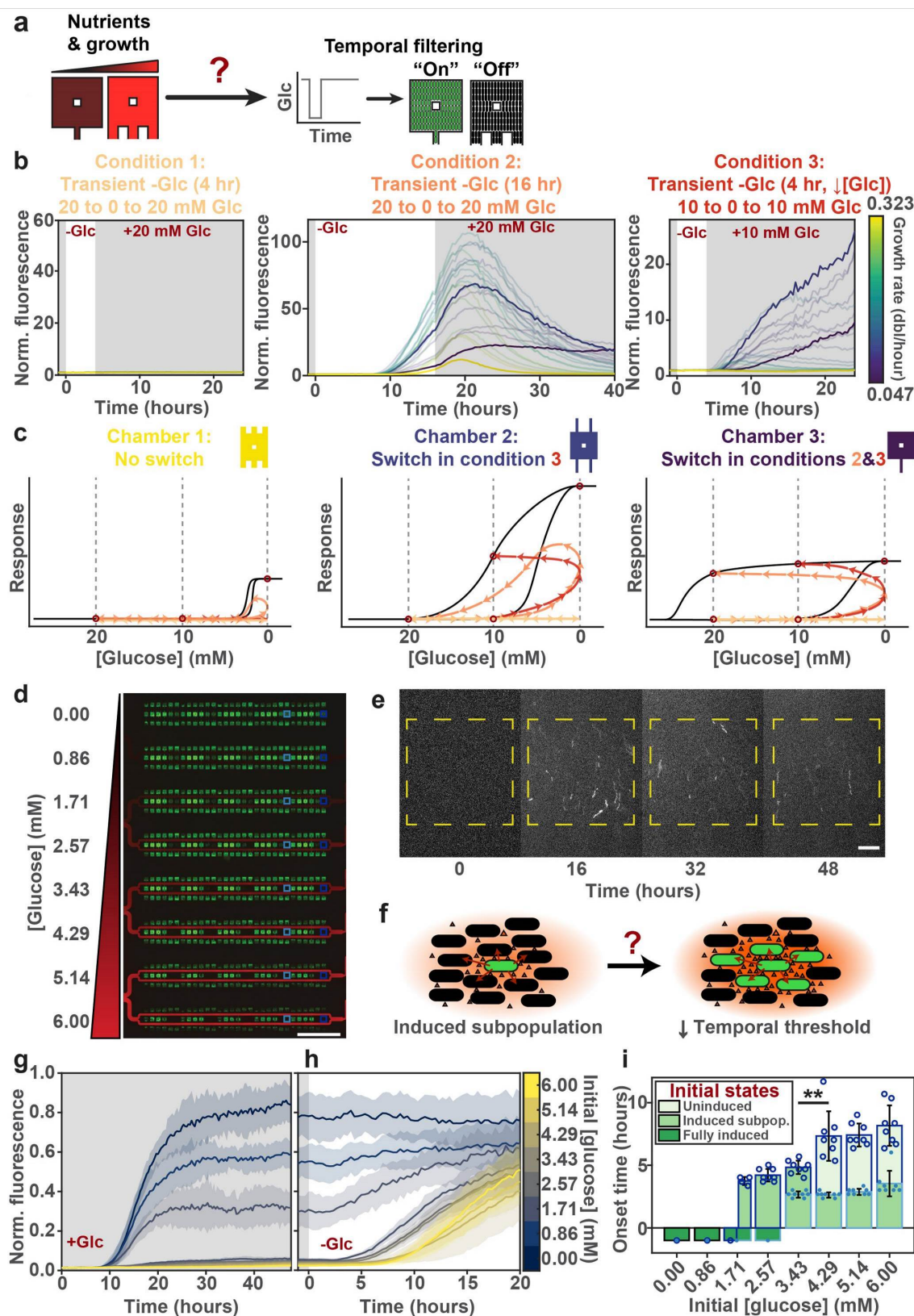909   **Figure 4 Sensitivity to environmental change as encoded in the form of a temporal**

910   **threshold can be enhanced with cell signaling. a,** QS onset can be controlled by a condition-

911   dependent temporal threshold during transient stimulation. **b,** Response dynamics of 4 hour

912   transient glucose (20 mM) removal (condition 1), 16 hour transient glucose (20 mM) removal

913   (condition 2), and 4 hour transient glucose (10 mM) removal (condition 3). All conditions were

914   in tryptone medium at 25°C. (mean, n = 6, from 3 independent experiments). 3 sample chambers

915   in each condition have been highlighted. **c,** Theoretical hysteretic diagrams of three sample

916   chambers within the three conditions in **b. d,** Fluorescence micrograph of gradient-generating

917   device, with chambers of interest indicated in blue boxes and the gradient visualized in red. Scale

918   bar, 1 mm. **e,** Filmstrip of a representative chamber exposed to 2.57 mM glucose demonstrating

919   maintenance of a stably induced subpopulation over ~40 hours. Scale bar, 20 μm. **f,** Proposed

920   effects of an induced subpopulation. **g,** Response dynamics from chambers exposed to 0 – 6 mM

921   linearly graded glucose concentrations over 48 hours (n = 8). **h,** Response dynamics over 24

922   hours after glucose removal (n = 8). **i,** Onset time of chambers exposed to different initial

923   concentrations of glucose. (n = 8, **$**P<0.01$, two tailed Student's *t*-test). (mean ± SD)